EMBEDDING LEARNING FOR APPROXIMATING PERSON-SPECIFIC COGNITIVE SIMILARITY : FOCUSING ON MEDICAL IMAGES

Anonymous authors
Paper under double-blind review

ABSTRACT

Metric learning is often applied in scenarios where labels are well-defined or where there is a ground truth for semantic similarity between data points. However, in expert domains such as medical data, where experts perceive features and similarities differently on an individual basis, modeling psychological embeddings at the individual level can be beneficial. Such embeddings can predict factors that influence behavior, such as individual uncertainty, and support personalized learning strategies. Despite this potential, the amount of person-specific behavioral data that can be collected through similarity behavior sampling is insufficient in most scenarios, making modeling individual cognitive embeddings challenging and underexplored. In this study, we proposed integrating supervised learning on small-scale similarity sampling data with unsupervised autoencoder-based manifold learning to approximate person-specific psychological embeddings with significantly improved similarity inference performance. We conducted a large-scale experiment with 121 clinical physicians, measured their cognitive similarities using medical image data, and implemented person-specific models. Our results demonstrate that even in complex expert domains, such as medical imaging, where cognitive similarity varies between individuals, person-specific psychological embeddings can be effectively approximated using limited behavioral data.

1 INTRODUCTION

Deep machine learning (ML) models can provide abstract-level information regarding the similarity between data through embedding (Liu et al., 2020b; Bengio et al., 2013; Mikolov et al., 2013). For instance, samples positioned close together in the embedding space can be interpreted as semantically similar, whereas those that are far apart are different. However, the actual similarity between the samples may not always be reflected in the learned embedding of the model. Metric learning is a method in which a model learns a function of the actual similarities and differences between samples and fits this function to low-dimensional embedding. In this context, the 'actual similarity' refers to a conventional metric that is defined externally. For example, in labeled datasets, a clear metric states that data points with the same label should be closer to each other than those with different labels. Even in the absence of labels, many datasets have commonly accepted metrics, such as the general perception that dogs are more similar to cats than snakes. Most metric-learning approaches operate under such conditions; thus, sufficient training data are available.

By contrast, we introduce a specialized metric learning problem that approximates individual-level psychological (cognitive) embeddings in scenarios where there are significant differences in similarity metrics depending on the individual (Schroff et al., 2015; Liu et al., 2017; Hosseini et al., 2018; Luo et al., 2003). This issue is particularly relevant in expert-driven fields such as medical data, where interpretations often differ. For example, while chest X-ray (CXR) images are structurally simple, their interpretation is highly complex (Delrue et al., 2011; Pham et al., 2021). Even among experienced physicians, the cognitive similarities or diagnoses of CXR images can vary widely (see Section 3.3) (Krupinski, 2010). Moreover, because labels are defined using partial data features, they may not align with the similarities assessed from a holistic perspective. For example, in CXR data, it may be necessary to differentiate between 'Male' and 'Female,' while also distinguishing be-

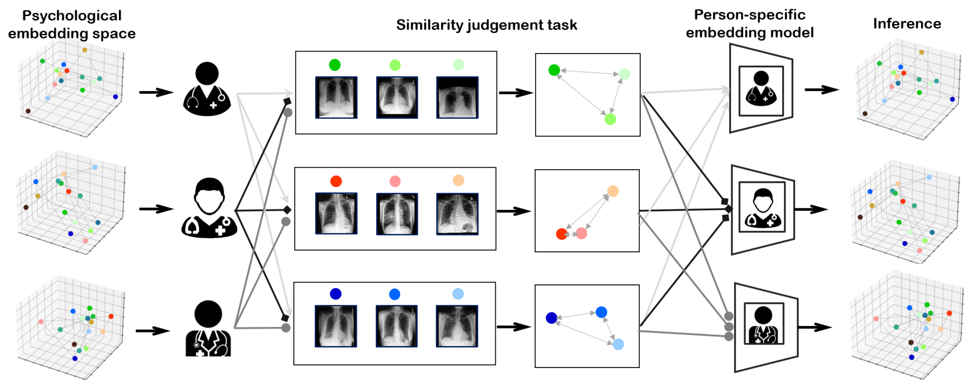

Figure 1: Illustration of the person-specific cognitive embedding modeling framework. Individual similarity measurement experiments arrange three images into a scalene triangle based on their pairwise similarities. This similarity data is then converted into triplets to train a person-specific embedding model. The resulting model approximates the person's psychological embeddings.

tween 'Normal' and 'Abnormal'. Therefore, in highly complex datasets, an individual's perception of similarity can remain independent of external metrics (labels).

This scenario is important because approximating individual-level cognitive metrics with psychological embeddings enables the inference of features considered more important by each person. Personalized learning strategies can be developed by identifying areas with high uncertainty because similar data points often exhibit similar uncertainties (Liu et al., 2020a; Mukhoti et al., 2021; Sanchez et al., 2022). This approach can also improve expert AI by transferring the psychological representations of superior experts to models.

Therefore, it is important to attempt to approximate cognitive embedding at the individual level; however, such attempts are rare. The biggest challenge lies in the inherent noise and difficulty of obtaining sufficient behavioral sampling for individual-level psychological embedding modeling (Molenaar & Campbell, 2009). In practical scenarios, modeling individual-level psychological embeddings requires overcoming the issue of insufficient behavioral sampling. As an alternative, we demonstrated that by integrating a loss function that learns from behavioral sampling data collected from individuals into an autoencoder-based framework, it is possible to synergistically achieve person-specific psychological embedding modeling that represents cognitive similarity, even with a limited amount of training data.

Our objective is not to improve metric learning algorithms or optimize models but to propose and experimentally validate a practical approach for applying metric learning to individual embedding learning. Specifically, we conducted a first-ever behavioral sampling experiment to measure the cognitive similarity of actual CXR images with 121 clinical physicians, focusing on realistic scenarios. After confirming significant variations in the cognitive similarity patterns across individuals, we implemented autoencoder-based models to represent each person's similarity metric at the embedding level (Fig. 1). The performance of the model was evaluated using individual behavioral data, and the robustness of our hypothesis was validated through ablation studies and simulations.

The key contributions of our study are as follows:

1) This is the first expert-based experimental study to model individual-level psychological embeddings, demonstrating the applicability of our approach to a realistic scenario using actual clinical physicians and medical data. 2) We showed that autoencoders can synergistically complement the limitations of cognitive similarity sampling in individual-level cognitive similarity approximations. (Proposing a new application scenario for autoencoders) Additionally, we empirically demonstrated the utility of the variable triplet loss, which was proposed to learn the psychological embeddings in the bottleneck layer of the autoencoder. 3) The experiment, which involved 121 physicians and medical imaging data, required considerable time and effort. The raw experimental data will contribute to research in fields such as human–AI collaboration.

2 Related Work

2.1 Metric learning

This study is closely related to metric learning in ML, which involves training models to learn the similarity between samples (Weinberger & Saul, 2009; Xing et al., 2002; Weinberger et al., 2005). Early algorithms focused on discriminating similar and dissimilar samples or with pre-defined metrics (Aherne et al., 1998; Elgammal et al., 2003). Recent approaches aims to learn the distance function in the embedding space of the model, representing similar and dissimilar samples as close and distant, respectively. For instance, selecting a reference image (anchor) among three data points helps determine which one is closer or farther from the reference, referred to as triplets (Hoffer & Ailon, 2015; Wang et al., 2017; Le-Khac et al., 2020; Ge, 2018; Hoffer & Ailon, 2015; Kim et al., 2020). Consequently, the triplet loss that reflects the conditions of these triplets in embedding space can be defined. It increases the distance between negative pairs more than the positive pairs. From the perspective of metric learning, the goal of our work is not to improve existing algorithms but rather to apply metric learning to model person-specific psychological metrics, which are not defined externally. This distinguishes our work from other studies.

2.2 Person-specific cognitive similarity modeling

Human inference operates through cognitive mechanisms that can be conceptualized as a hypothetical representational space, analogous to embeddings in machine learning models. In cognitive science, this representational framework is referred to as a psychological embedding. According to the theory of similarity-representation duality, embedding models trained on an individual's cognitive similarity metrics can concurrently encapsulate their cognitive features (Roads & Love, 2024). This framework suggests that similarity metrics specific to an individual can uncover the relative weighting of features involved in their perceptual processing of objects. By harnessing these insights, personalized embedding models have the potential to identify optimal learning domains and highlight knowledge deficits in experts (Cha & Lee, 2021).

Previous research in cognitive science has investigated tasks pertinent to the development of individualized embeddings. These efforts include systematic evaluations of human perceptual characteristics (Zhang et al., 2018), fine-tuning neural networks to enhance predictions of human similarity judgments (Tarigopula et al., 2023), and integrating neurological signals with cognitive embeddings (Palazzo et al., 2020). Although substantial progress has been achieved in collecting behavioral data for psychological embeddings across diverse stimuli (Hebart et al., 2020; Nosofsky et al., 2018; Wilber et al., 2014), relatively few studies have addressed the technical challenges associated with insufficient sampling for individual-level modeling. To address this gap, our study investigates the potential of leveraging unsupervised learning techniques, specifically autoencoders, to amplify limited person-specific similarity information.

In contrast to conventional metric learning frameworks that rely on predefined, consensus-based similarity metrics, person-specific metric learning becomes particularly valuable in contexts such as expert-driven domains, where cognitive similarity metrics exhibit significant inter-individual variation. Nevertheless, most prior study in this area has relied on benchmark datasets characterized by relatively minor differences in individual similarity perceptions (Peterson et al., 2018). Our work presents a novel contribution by validating the feasibility of individualized embedding modeling in real-world, professional datasets such as medical imaging, thereby bridging theoretical cognitive science and practical expert applications.

2.3 Autoencoder and manifold learning

Autoencoders learn the latent representations of data points in the bottleneck layer between the encoder and decoder by minimizing the reconstruction loss of the decoder for the input data (Berahmand et al., 2024; Tschannen et al., 2018; Wang et al., 2014). The objective is to learn latent representations and thereby discover hidden structures in the data. From the perspective of the manifold theory, training an autoencoder is equivalent to determining the parameters of a data manifold (Lempitsky, 2019; Lu et al., 2019). However, manifold structures are not always singular and it is common for data to belong to multiple manifolds (Hettiarachchi & Peters, 2015). Although the robustness of autoencoders has been demonstrated in numerous studies, explaining the local structure

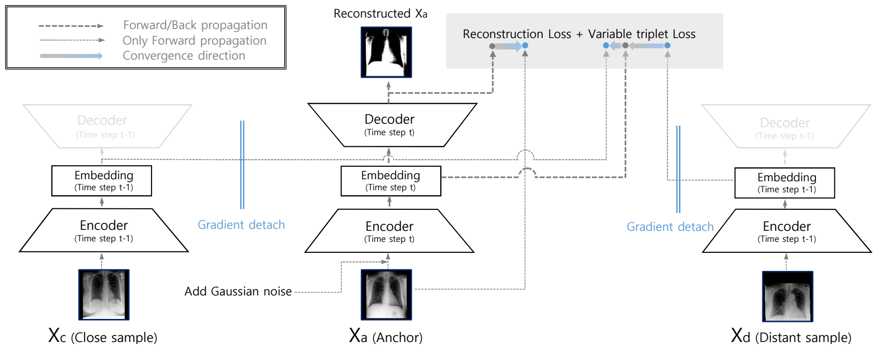

Figure 2: Illustration of the loss structure and its optimization process on a synthetic example.

of the manifolds represented in the embedding space learned by unconstrained autoencoders remains challenging (Tschannen et al., 2018). Instead, autoencoders can potentially learn various manifold structures depending on the initial weights of the model or certain constraints. If we assume that each individual's psychological embedding space represents a manifold, autoencoders can offer a useful guide for modeling person-specific psychological embeddings. However, this approach has not been explored previously.

3 Approach

3.1 Collecting similarity judgements

Sampling behavioral data for person-specific modeling may entail several limitations. First, behavioral data from a subject can typically only be used to train an individual model for that subject. Considering the laborious nature of behavioral sampling, the collection of triplets can incur high costs. Consequently, the amount of behavioral data that can be gathered from a single individual may be limited. Second, although the dimensionality of the embedding space is lower compared to the stimulus (i.e., raw images) space, it remains high-dimensional, posing challenges in case of intuitive handling (Roads & Love, 2024). This dimensionality can introduce significant noise when measuring similarity between data points. We implemented a triangular measurement framework treating each data point composing a triplet as an independent anchor to collect efficient behavioral data with minimal sampling and low uncertainty. Considering three data points, the selection of one of them as the anchor forms a unmeasured triplet $\mathcal{T} = (\mathbf{x}_a, \mathbf{x}_1, \mathbf{x}_2)$, where $\mathbf{x}_a$ denotes the anchor point, and $\mathbf{x}_1$ and $\mathbf{x}_2$ denote the other points, respectively. When the subject $\mathbf{s}$ selects a data point that is either more similar or dissimilar to $\mathbf{x}_a$ from $\mathbf{x}_1$ and $\mathbf{x}_2$, the $\mathcal{T}$ is expressed as the 'measured triplet' $\mathcal{T}^{\mathbf{s}} = (\mathbf{x}_a, \mathbf{x}_c, \mathbf{x}_d)$, where $\mathbf{x}_c$ and $\mathbf{x}_d$ denote the close and distant points, respectively, based on the behavioral measurements of the subject $\mathbf{s}$. Therefore, each measured triplet has two possible labels. Excluding the anchor, the remaining two images in a triplet are labeled as one close ("close" sample) and one relatively distant ("distant" sample). In our measurement procedure, three images were presented to the participant without specifying any anchors. Subsequently, the subject arranged the positions of these images in a scalene triangle shape, reflecting the degree of closeness or distance between each pair of images. Upon fixing the anchor image, a triplet was automatically determined with the remaining two images. Therefore, with three images presented in one instance, three triplets were collected. Thus, considering three data points sampled from the entire dataset without duplication m times, m measurement experiment instances can be conducted, thereby yielding $3m$ triplets. Although the triplets obtained from a single instance may be interdependent, this approach could regularize subject response by reducing the degree of freedom in representing cognitive distances between data points. Moreover it facilitates the collection of three sets of behavioral data from a single experiment, thereby enhancing sampling efficiency.

3.2 Convolutional autoencoder with variable triplet loss

Cognitive representation may rely on biological parameters such as neurological architecture (Kriegeskorte, 2015; Kubilius et al., 2018), suggesting the importance of considering suitable ML model architectures and loss functions. However, to the best of our knowledge, a generally applicable ML architecture that can emulating psychological embeddings has not been proposed. Therefore, we empirically designed the embedding model architecture based on convolutional autoencoder (Chen et al., 2017) considering the context of medical image modeling without labels. Its architecture offers several advantages for our objectives. First, convolutional neural networks (CNN) are considered viable for modeling visual perception to date (Zeiler & Fergus, 2014). Second, the collection of sufficient data for training deep CNNs with numerous parameters through individual behavioral sampling can pose challenges. Autoencoders (unsupervised embedding learning methods) can partially address the insufficient behavioral data issue by directly extracting a meaningful feature independent of classes (Yang et al., 2022; Psenka et al., 2024; Bank et al., 2023).

The proposed autoencoder model comprises an encoder $\mathbb{E}(\cdot)_t$ and decoder $\mathbb{D}(\cdot)_t$, each comprising convolution and deconvolution layers, respectively, where t denotes training iteration step (i.e., epoch). The fully connected bottleneck layer, serving as the output of the encoder and input of the decoder, was designed to approximate the region of interest, psychological embeddings. Consider images $\{\mathbf{x}, \cdots\}$ and the corresponding embeddings output of the encoder $\{\mathbb{E}(\mathbf{x})_t, \cdots\}$, where $\mathbb{E}(\mathbf{x}) \in \mathbb{R}^D$ denotes the D-dimensional vector. At each training iteration, we randomly sampled a batch of measured triplets among the training set (Refer to Sec. 3.4). Training aims to prompt an increase in the Euclidean distance between $\mathbb{E}(\mathbf{x}_d)_t$ and $\mathbb{E}(\mathbf{x}_a)_t$ compared to the distance between $\mathbb{E}(\mathbf{x}_c)_t$ and $\mathbb{E}(\mathbf{x}_a)_t$, while the autoencoder reconstructs the input $\mathbf{x}_a$. Thus, we aimed to minimize the following loss function for each subject $\mathbf{s}$'s model at iteration t.

$$\mathcal{L}_{tri}(\mathcal{T}^{\mathbf{s}})_t = \underbrace{\|\mathbb{D}(\mathbb{E}(\mathbf{x}_a + \epsilon)_t)_t - \mathbf{x}_a\|_2}_{\text{recontruction loss}} + \underbrace{\alpha\|\mathbb{E}(\mathbf{x}_a)_t - \widehat{\mathbb{E}(\mathbf{x}_c)_{t-1}}\|_2 + \beta\|\mathbb{E}(\mathbf{x}_a)_t - \widehat{\mathbb{E}(\mathbf{x}_d)_{t-1}}\|_2}_{\text{variable triplet loss}}, \tag{1}$$

where $\|\cdot\|_2$ denotes L2-norm, ϵ is Gaussian random noise, α and β are hyperparameters that satisfy $\alpha > \beta$, and $\widehat{\cdot}$ denotes a constant tensor with no gradient flow. Further, $\mathbb{E}(\mathbf{x}_c)_{t-1}$ and $\mathbb{E}(\mathbf{x}_d)_{t-1}$ function as candidate vectors for embedding the subject for $\mathbf{x}_c$ and $\mathbf{x}_d$, respectively, indicating the convergence target of $\mathbf{x}_a$ at iteration t. However, with training progression, the candidate vectors for embedding change, rendering the overall convergence target of the loss function variable. A weakening in the convergence of stochastic gradient descent is anticipated, but with properly selected hyperparameters like learning rate, batch size, α, and β, optimization primarily depends on reconstruction loss, minimizing significant convergence issues. Although autoencoders can effectively learn compressed representations, they are prone to overfitting and encounter challenges when determining feature importance (Meng et al., 2017). The variable triplet loss can be interpreted as constraints guiding the training of autoencoders towards the identification of features that are more specific to the target individual among the candidate features they can explore (Fig. 2).

3.3 Person-specific similarity pattern quantification

To quantitatively express and compare the cognitive similarities among subjects participating in experiments for the same dataset, we defined **similarity pattern vector (SPV)**. Assume that we collected behavioral datasets through multiple instances m times from subject $\mathbf{s}$. This formed a set $\mathsf{T}^{\mathbf{s}}_{\Omega}$ comprising $3m$ triplets. Each element triplet $\mathcal{T}^{\mathbf{s}}_i$ ($\forall i \in \{1, \cdots, 3m\}$) composing $\mathsf{T}^{\mathbf{s}}_{\Omega}$ can be transformed into binary labeling. Therefore, assuming each triplet as an independent dimension determining the similarity pattern of the subject $\mathbf{s}$, the similarity pattern is defined as follows.

$$SPV(\mathsf{T}^{\mathbf{s}}_{\Omega}) = [\mathbb{O}(\mathcal{T}^{\mathbf{s}}_1), \mathbb{O}(\mathcal{T}^{\mathbf{s}}_2), \cdots, \mathbb{O}(\mathcal{T}^{\mathbf{s}}_{3m})], \tag{2}$$

where $\mathbb{O}(\mathcal{T}^{\mathbf{s}}_{\mathbf{n}})$ denotes one of the possible similarity relationships for the $\mathbf{n}$-th $\mathcal{T}^{\mathbf{s}}$, expressed as 1 for one relation and 0 for another. Thus, $SPV(\mathsf{T}^{\mathbf{s}}_{\Omega})$ is the $3m$-dimensional one-hot vector expression, which indicates the person-specific similarity pattern.

3.4 Training and evaluation of the model

The triplet set $\mathsf{T}^{\mathbf{s}}_{\Omega}$ was randomly assigned to the training set $\mathsf{T}^{\mathbf{s}}_{\mathbf{T}}$, validation set $\mathsf{T}^{\mathbf{s}}_{\mathbf{V}}$, and evaluation set $\mathsf{T}^{\mathbf{s}}_{\mathbf{E}}$ according to a predetermined ratio. While optimizing Eq. 1 using $\mathsf{T}^{\mathbf{s}}_{\mathbf{T}}$, the optimal model was determined considering the highest inference accuracy achieved on $\mathsf{T}^{\mathbf{s}}_{\mathbf{V}}$. Further, to address the scenario wherein inference accuracy must be treated across various models, we defined a predictive evaluation function $\mathcal{F}$ for single triplet $\mathcal{T}_{\mathbf{i}}^{\mathbf{s}}$ as follows.

$$\mathcal{F}\left(\mathbb{E}_{\mathbf{j}}(\mathbf{x}), \mathcal{T}_{\mathbf{i}}^{\mathbf{s}}\right) = \begin{cases} 1, & \text{if } \|\mathbb{E}_{\mathbf{j}}(\mathbf{x}_a) - \mathbb{E}_{\mathbf{j}}(\mathbf{x}_d)\|_2 > \|\mathbb{E}_{\mathbf{j}}(\mathbf{x}_a) - \mathbb{E}_{\mathbf{j}}(\mathbf{x}_c)\|_2 \\ 0, & \text{otherwise} \end{cases}, \tag{3}$$

where, $\mathbb{E}_{\mathbf{j}}(\mathbf{x})$ is output over fed $\mathbf{x}$ of the encoder trained using $\mathsf{T}_{\mathbf{T}}^{\mathbf{j}}$ and $\mathsf{T}_{\mathbf{V}}^{\mathbf{j}}$, $(\mathbf{x}_a, \mathbf{x}_c, \mathbf{x}_d)$ is $\mathcal{T}_{\mathbf{i}}^{\mathbf{s}}$.

In case of considerable diversity in cognitive patterns among subjects, (Sec.4.3) a model trained on $\mathsf{T}_{\mathbf{T}}^{\mathbf{i}}$ is strongly expected to achieve higher performance on $\mathsf{T}_{\mathbf{E}}^{\mathbf{i}}$. Whereas, the performance on $\mathsf{T}_{\mathbf{E}}^{j}$, (for $j \neq \mathbf{i}$), should be lower compared to $\mathsf{T}_{\mathbf{E}}^{\mathbf{i}}$. We defined the performance measured on the evaluation set comprising h triplets obtained from the target subject $\mathbf{j}$ of the model as **Specific Performance (SP)** : $(\Sigma_{i=1}^{h}\mathcal{F}\left(\mathbb{E}_{\mathbf{j}}(\mathbf{x}), \mathcal{T}_i^{\mathbf{s}}\right))/h \times 100$ $(i = 1, \cdots h)$. Further, the performance measured on the test set collected from all g subjects measured with the $\mathsf{T}_{\mathbf{E}}$ except the target subject $\mathbf{j}$ of the model was defined as **Non-Specific Performance (NSP)** : $(\Sigma_{k=1}^{g}\Sigma_{i=1}^{h}\mathcal{F}\left(\mathbb{E}_k(\mathbf{x}), \mathcal{T}_i^{\mathbf{s}}\right))/h(g-1) \times 100$ $(i = 1, \cdots h, k = 1, \cdots g, k \neq \mathbf{j})$. Note that the reliability of NSP improves with a larger experimental group size since NSP depends on the subject group.

3.5 Qualitative Analysis

The performance of the embedding model can be qualitatively evaluated by comparing the locations of the top n pixels predicted by the model to influence similarity judgments with the n pixels identified by experienced clinicians. The annotation process of the model begins by selecting a reference unit with the highest variance among the embedding outputs of a separate reference dataset. Once the reference unit is determined, uniform noise is iteratively added to each pixel of the test image, which is then input into the model to compute the variance in the reference unit's output. This process is conducted individually for each pixel (Sec. A.6). Subsequently, the top n pixels that caused the greatest variance in the reference unit's output due to the added noise are identified and compared with the pixels annotated by expert clinicians.

4 Experiments

Herein, we describe the human behavioral experiment setup and dataset (Sec. 4.1.-4.2) and present evidence that the similarity perception patterns of physicians vary on an individual basis (Sec 4.3). Then we evaluate the predictive performance of embedding models trained on a person-specific basis (Sec 4.5). We provide evidence that the performance of embedding models can improve with the scale of behavioral sampling through human surrogate model simulations (Sec. 4.7). Additionally, we examine the significance of each term of loss function through ablation study (Sec. 4.8).

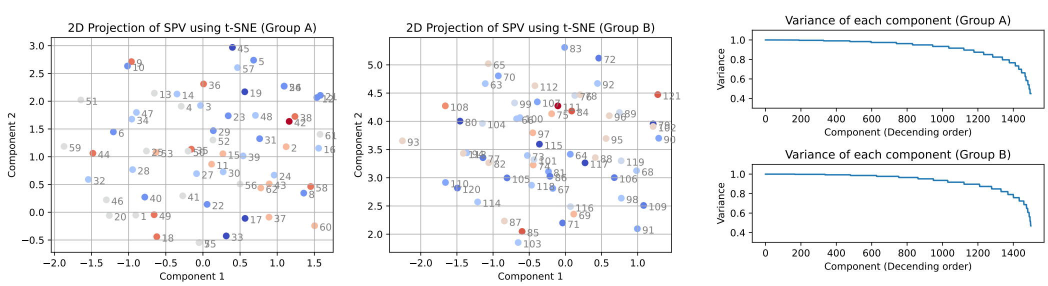

(a) (b)

Figure 3: Results of group-based similarity pattern analysis for all subjects. (a) 2D t-SNE visualization of similarity pattern vectors (SPVs). The colors represent the results of a separate image interpretation test conducted with the subjects, where red indicates relatively higher performance. (b) Variance of components in the SPVs (Decending order).

4.1 Datasets

CXR images serve as a crucial diagnostic modality in all clinical fields owing to their capability to contain wide clinical information. Moreover, interpreting CXR images can be challenging even

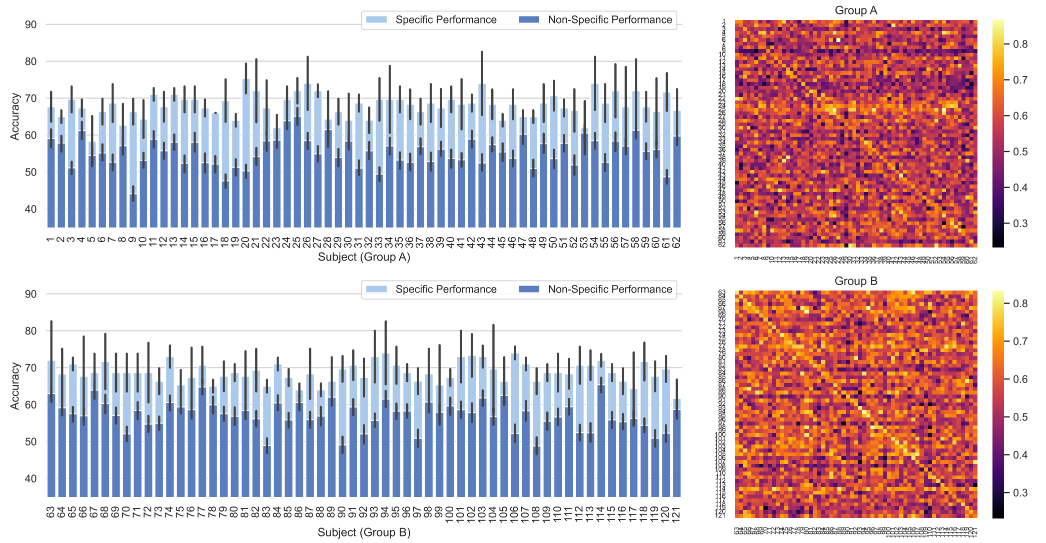

(a) (b)

Figure 4: Similarity inference performance analysis. (a) Model-specific results (Accuracy: %, bar: standard deviation). (b) Cross-performance heatmap (X-axis: subject triplets, Y-axis: models).

for experienced clinicians, and they may have diverse similarity perception patterns. This scenario aligns well with our task objectives. To compensate the limitations of single-domain experiments, we constructed two different experimental datasets. The CXR-A dataset was formed via random sampling of images labeled as 'Normal' or 'Abnormal' from the CheXpert 1.0 dataset (Irvin et al., 2019), whereas the CXR-B dataset comprised images labeled as 'Edema' or 'Pneumonia' from the same source. In our experiments, labels were unnecessary; however, we used this approach to sample the two sub-datasets from different distributions. Each dataset comprised 500 subsets, with each subset comprising three images (Therefore, resulting $\mathcal{T}^{\Omega}$ comprised 1500 $\mathcal{T}$ after the subject similarity measurements). CXR-A images might not clearly show lesions, leading physicians to focus on overall anatomical outlines, whereas CXR-B images, with more evident lesions, may lead physicians to focus on pathology (Behzadi-Khormouji et al., 2020; Homayounieh et al., 2021).

4.2 Human experiments for similarity measurement

We conducted experiments with 121 government-licensed clinical physicians, recruited from the official medical association. After randomly selecting 150 subjects, 121 were included, excluding those who withdrew. Subjects were assigned to Group A (1-62) and Group B (63-121), with each group using CXR-A and CXR-B, respectively. In the experiment, three unlabeled images (1 subset) were shown on the monitor, and subjects were asked to drag balls to indicate similarity, with closer balls representing more similarity. Despite a flexible scale between ball distances, the subjects were requested to maintain consistent criteria across all instances. The experiment had no time limit, and breaks were allowed. Group A took an average of 304 minutes to complete 500 experiments, while Group B took 245 minutes. Subsets were presented in a randomized order.

4.3 Similarity pattern comparison

Fig.3 (a) shows the t-SNE (Van der Maaten & Hinton, 2008) dimensionality reduction of the SPV (Eq.2) from the all subjects over belonging group. Each component of SPV was formed by all 1500 triplets collected from each subject. The similarity patterns among subjects from both groups were diverse, and did not form clusters. In the multivariate runs test conducted to assess randomness, SPV demonstrated randomness with p-values of 0.18 and 0.07 for the CXR-A and CXR-B groups, respectively. Thus, individuality embedding modeling for each person is necessary. Fig. 3 (b) illustrates the variance of each component of the the SPV across all subjects (descending order).

Despite the high variance in most components, the presence of components with relatively low variance suggested the potential of partial similarity patterns generally shared by subjects.

4.4 MODELING DETAIL

The best model architecture designed herein comprised an encoder with four convolutional layers, and a decoder with four deconvolutional layers (See A.2). All results, except for the comparative experiment (ablation study) presented in Sec. 4.8, are reported based on the best architecture. The embedding layer (region of interest), was a one-dimensional tensor with 64 units. Original gray images of size 1024×1024 presented to subjects were reduced to $(1\times128\times128)$ and employed as model input data. We employed the PyTorch (Paszke et al.) for all experiments. We fixed the learning rate to 10^{-4} and used the Adam optimizer (Kingma & Ba, 2014) with 32 mini-batch size. The hyperparameters for training were consistent across all models. α and β were set to 1.2 and 1, respectively; however, they were fine-tuned by the algorithm to reflect the distance scale reported by the subjects during the experiment.

4.5 PERFORMANCE OF PERSON-SPECIFIC SIMILARITY INFERENCE (MAIN STUDY)

Fig. 4 (a) shows the SP and NSP of all individual models. The number of triplets for training, validation, and evaluation was randomly set to 1410, 60, and 30, respectively. The final performance was reported using 3-fold cross-validation with random selection. Our models achieved significantly higher SP (Group A average 68%, Group B average 68.7%) compared to the chance level, thereby validating the efficacy of our approach. Considering the diverse similarity patterns among subjects, models may exhibit lower predictive performance on evaluation triplets of different subjects.(Models should achieve specific strong performance for test triplets for corresponding subject) Notably, across all models, a consistent trend of the NSP being lower than SP as observed. Fig. 4 (b) presents the cross-predictive performance on a heat-map for person-specific models on the evaluation triplets for all subjects. While displaying distinct predictive tendencies specific to the target subject's evaluation data, the models demonstrated random patterns for the data of the non-corresponding subjects, thereby aligning with the similarity patterns in the group (Sec. A.5).

4.6 RESULTS OF QUALITATIVE ANALYSIS (SUB-STUDY)

Figure 5 illustrates examples of the top 10 image regions where changes in pixel values influenced similarity, as determined by the procedure described in Section 3.5. The annotations shown on the left image were performed by experienced clinicians. The regions affecting experts' similarity judgments differed between CXR-A and CXR-B. In CXR-A, similarity judgments were primarily influenced by anatomical structures such as bones and the thorax, whereas in CXR-B, regions around lung lesions played a key role. These tendencies were also reflected in the annotations generated by the proposed model. Table 1 summarizes the proportion of pixels, averaged across all subjects, where the top 10 similarity-determining pixels predicted by the model were within a 2-inch distance of the 10 pixels identified by experienced clinicians. The proposed model demonstrated patterns closely aligned with those of the experts, while the comparative model (a conventional autoencoder described in Section 4.8) exhibited significantly weaker predictive performance.

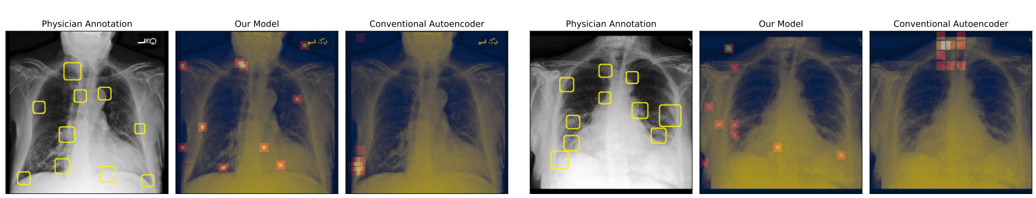

(a) Example of CXR-A test image 1 (Subject 2)   (b) Example of CXR-B test image 1 (Subject 68)

Figure 5: Annotation of image regions where changes in pixel values impact embedding similarity.

Table 1: Proportion of top 10 similarity-determining pixels within 2 inches of expert annotations (CA : Conventional autoencoder).

CXR-A Test Image 1 (n=62)		CXR-A Test Image 2 (n=62)		CXR-B Test Image 1 (n=59)		CXR-B Test Image 2 (n=59)	
Our Model (%)	CA (%)	Our Model (%)	CA (%)	Our Model (%)	CA (%)	Our Model (%)	CA (%)
49.3±17.1	13.8 ±12.7	50.8±10.9	14.8±9.7	51.0±17.2	22.8 ±12.3	45.4±14.5	18.9±11.8

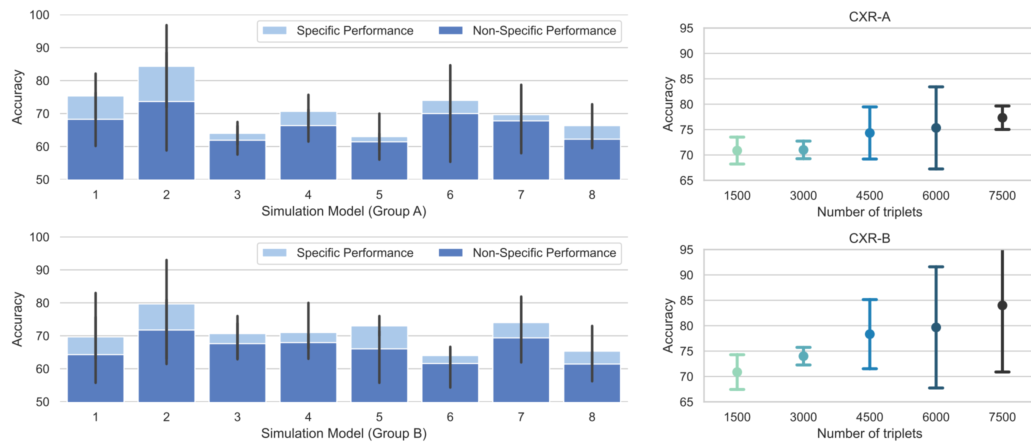

(a) (b)

Figure 6: Inference performance of simulation experiments. (a) Model-specific results (Accuracy: %, bar: Standard deviation). (b) Effect of amount of triplets in simulation (bar: standard deviation).

4.7 Simulation experiments

We showed that the embeddings of the original model could be reconstructed in preserved similarity even in simulations wherein the subjects were replaced with ML models. We sampled 100 images each from CheXpert, which were not included in CXR-A or CXR-B. Thereafter, 16 different binary classification CNN models were trained for each set. We measured the Euclidean distance of output vectors inner layer immediately before the final layer for each model for the same triplets as in the human behavioral experiments to collect the similarity relationship. Subsequently, the secondary embedding model was trained in the same manner of the modeling of human embedding (Fig. 6 (a)). The performance was slightly higher than that in human behavioral experiments, indicating that noises may occur in the similarity measurement process for human subjects. Moreover, in the experiments wherein the number of subsets for CXR-A and CXR-B was increased using additional data, the performance of the embedding model for simulation exhibited an improvement according to the number of triplet samples for model training (Fig. 6 (b)). Thus, this implies increasing human behavioral experiment sample sizes could enhance embedding model performance in future.

4.8 Ablation and comparison study

This section summarizes the study designed to demonstrate the effects of the proposed modeling approach components on the loss function. Table 2 shows the inference performance of models trained by excluding each component (reconstruction and variable triplet losses) while maintaining the same training settings as in our proposed method. In both the ablated settings, the performance exceeded the chance level; however, it was lower than that of our proposed setting. An important finding is that the setup excluding variable triplet loss (i.e., conventional autoencoder) surpasses the opposite setting. It shows prioritizing reconstruction loss optimization offers advantages for embedding learning over exclusively optimizing triplet loss. This implied the presence of common latent similarity patterns among subjects that can be learned solely by autoencoders and indicated that the features that cannot be trained through triplet loss alone owing to sampling limitations were trained via the optimization of the reconstruction loss of the autoencoder. Moreover, in the ablation set-

Table 2: Results of ablation study (error: standard deviation).

Methods	Group A (n=62)		Group B (n=59)	
	SP (%)	NSP (%)	SP (%)	NSP (%)
Autoencoder with variable triplet loss (Our methods)	68.0±3.2	55.5 ±3.9	68.8±2.7	57.2±3.8
Variable triplet loss only (Excluding recontruction loss)	53.9±8.0	53.8±3.8	55.7±5.0	55.0±4.8
Autoencoder only (Excluding variable triplet loss)	57.9±6.0	56.8±3.8	62.3±4.8	59.7±3.1
Encoder with triplet loss (Excluding decoder)	61.8±3.1	56.3±2.8	60.7±4.5	57.0±4.1
Encoder only (Excluding decoder and variable triplet loss)	62.3±3.4	55.3±3.3	60.9±4.0	56.0±3.5

ting, SP was marginally higher than NSP; however, no significant superiority was observed, thereby suggesting an incapability to extract person-specific features. Meanwhile, an ablation experiment was conducted by adding a classifier to the encoder of the autoencoder, utilizing cross-entropy loss alongside variable triplet loss. In this ablation experiment aimed at validating the utility of the decoder, the performance was higher than that of the variable triplet loss-only setting; however, it did not surpass the performance of our proposed method. In summary, these evidences support our claim that variable triplet loss guides person-specific feature learning in autoencoders.

5 Limitation

While pioneering person-specific similarity-based cognitive embedding, this study faces limitations inherent to human behavioral experiments, such as uncertainty in similarity judgments and interdependent measurements. Future studies should adopt systematic experimental designs to address this noise. Additionally, our experiments focused on a limited set of neural network architectures and did not explore optimal hyperparameter tuning or provide theoretical proof for the hypothesis that person-specific cognitive similarity can guide autoencoder manifold learning.

6 Conclusion

This study proposed an autoencoder-based person-specific embedding modeling framework that approximated cognitive similarities between subjects in CXR data and conducted a large-scale behavioral experiment with clinical physicians. To the best of our knowledge, this is the first such study attempt. Specifically, we demonstrated that our approach can be applied in domains where significant inter-observer variability in similarity perception exists, such as in the complex interpretation of CXR images. As our experimental design did not include any domain-specific constraints or assumptions unique to the medical field, we believe that our method can potentially be generalized to other domains.

We hypothesized that individual psychological embeddings reflect features learned independently of external metrics (such as labels). According to this hypothesis, information derived from high-dimensional data that is cognitively interpreted may lie on a lower-dimensional psychological manifold. Autoencoders probabilistically learn the data manifold independent of external metrics. Therefore, autoencoders may offer a useful framework for approximating human-metric-independent embeddings. We further suggest that triplet loss, which captures individual similarity, may have acted as a perturbation that guided the autoencoder toward learning a specific manifold. However, theoretical proof is beyond the scope of this study and should be explored in future studies. Additionally, through simulations and ablation studies using person surrogate models, we confirmed the robustness of the proposed method and demonstrated the potential for proportional improvements in the model inference performance as the scale of behavioral data sampling increases.

Our study, which uses a multidisciplinary approach that integrates cognitive science, machine learning, and expert knowledge applications, demonstrates the potential of aligning deep neural networks with human representational mechanisms as a tool for understanding human cognitive representations. This approach could also potentially contribute to the development of machine-learning algorithms that support personalized learning for experts. Future research will aim to provide theoretical proof for the hypothesis that variable triplet loss can guide manifold learning in autoencoders and enhance the scalability of the proposed method by applying various learning algorithms suggested in the field of metric learning.

7 Ethics Statement

We review several ethical issues that may arise in this study. This study was approved by the Institutional Review Board (IRB No. removed) to conduct experiments involving human subjects using medical data. Participants were compensated with an amount exceeding the legally mandated minimum wage. To address ethical concerns, particularly those arising from involving the general public in experiments using medical data, we intentionally restricted the participants to qualified professionals. All participants voluntarily provided informed consent. The detailed statistics of the participants are summarized in the Appendix. The images used in this study (CXR-A and CXR-B) were obtained from the publicly available CheXpert dataset and their use was reviewed in advance by the IRB. We carefully considered the potential ethical issues that could arise during the advancement of this study. Nonetheless, technologies predicting human cognitive characteristics may pose ethical challenges as they could expose the vulnerabilities of professionals, compromise their judgment through adversarial attacks, or lead to adverse selection by clients. Therefore, as this study advances, it may be necessary to address ethical considerations simultaneously.

References

Frank J Aherne, Neil A Thacker, and Peter I Rockett. The bhattacharyya metric as an absolute similarity measure for frequency coded data. *Kybernetika*, 34(4):363–368, 1998.

Dor Bank, Noam Koenigstein, and Raja Giryes. Autoencoders. *Machine learning for data science handbook: data mining and knowledge discovery handbook*, pp. 353–374, 2023.

Hamed Behzadi-Khormouji, Habib Rostami, Sana Salehi, Touba Derakhshande-Rishehri, Marzieh Masoumi, Siavash Salemi, Ahmad Keshavarz, Ali Gholamrezanezhad, Majid Assadi, and Ali Batouli. Deep learning, reusable and problem-based architectures for detection of consolidation on chest x-ray images. *Computer methods and programs in biomedicine*, 185:105162, 2020.

Yoshua Bengio, Aaron Courville, and Pascal Vincent. Representation learning: A review and new perspectives. *IEEE transactions on pattern analysis and machine intelligence*, 35(8):1798–1828, 2013.

Kamal Berahmand, Fatemeh Daneshfar, Elaheh Sadat Salehi, Yuefeng Li, and Yue Xu. Autoencoders and their applications in machine learning: a survey. *Artificial Intelligence Review*, 57(2): 28, 2024.

Yujin Cha and Sang Wan Lee. Human uncertainty inference via deterministic ensemble neural networks. In *35th AAAI Conference on Artificial Intelligence/33rd Conference on Innovative Applications of Artificial Intelligence/11th Symposium on Educational Advances in Artificial Intelligence*, pp. 5877–5886. ASSOC ADVANCEMENT ARTIFICIAL INTELLIGENCE, 2021.

Min Chen, Xiaobo Shi, Yin Zhang, Di Wu, and Mohsen Guizani. Deep feature learning for medical image analysis with convolutional autoencoder neural network. *IEEE Transactions on Big Data*, 7(4):750–758, 2017.

Louke Delrue, Robert Gosselin, Bart Ilsen, An Van Landeghem, Johan de Mey, and Philippe Duyck. Difficulties in the interpretation of chest radiography. *Comparative interpretation of CT and standard radiography of the chest*, pp. 27–49, 2011.

Ahmed Elgammal, Ramani Duraiswami, and Larry S Davis. Probabilistic tracking in joint feature-spatial spaces. In *2003 IEEE Computer Society Conference on Computer Vision and Pattern Recognition, 2003. Proceedings.*, volume 1, pp. I–I. IEEE, 2003.

Weifeng Ge. Deep metric learning with hierarchical triplet loss. In *Proceedings of the European conference on computer vision (ECCV)*, pp. 269–285, 2018.

Martin N Hebart, Charles Y Zheng, Francisco Pereira, and Chris I Baker. Revealing the multidimensional mental representations of natural objects underlying human similarity judgements. *Nature human behaviour*, 4(11):1173–1185, 2020.

Randima Hettiarachchi and James F Peters. Multi-manifold lle learning in pattern recognition. *Pattern Recognition*, 48(9):2947–2960, 2015.

Elad Hoffer and Nir Ailon. Deep metric learning using triplet network. In *Similarity-based pattern recognition: third international workshop, SIMBAD 2015, Copenhagen, Denmark, October 12-14, 2015. Proceedings 3*, pp. 84–92. Springer, 2015.

Fatemeh Homayounieh, Subba Digumarthy, Shadi Ebrahimian, Johannes Rueckel, Boj Friedrich Hoppe, Bastian Oliver Sabel, Sailesh Conjeti, Karsten Ridder, Markus Sistermanns, Lei Wang, et al. An artificial intelligence–based chest x-ray model on human nodule detection accuracy from a multicenter study. *JAMA Network Open*, 4(12):e2141096–e2141096, 2021.

Anahita Hosseini, Ting Chen, Wenjun Wu, Yizhou Sun, and Majid Sarrafzadeh. Heteromed: Heterogeneous information network for medical diagnosis. In *Proceedings of the 27th ACM International Conference on Information and Knowledge Management*, pp. 763–772, 2018.

Jeremy Irvin, Pranav Rajpurkar, Michael Ko, Yifan Yu, Silviana Ciurea-Ilcus, Chris Chute, Henrik Marklund, Behzad Haghgoo, Robyn Ball, Katie Shpanskaya, et al. Chexpert: A large chest radiograph dataset with uncertainty labels and expert comparison. In *Proceedings of the AAAI Conference on Artificial Intelligence*, volume 33, pp. 590–597, 2019.

Sungyeon Kim, Dongwon Kim, Minsu Cho, and Suha Kwak. Proxy anchor loss for deep metric learning. In *Proceedings of the IEEE/CVF conference on computer vision and pattern recognition*, pp. 3238–3247, 2020.

Diederik P Kingma and Jimmy Ba. Adam: A method for stochastic optimization. *arXiv preprint arXiv:1412.6980*, 2014.

Nikolaus Kriegeskorte. Deep neural networks: a new framework for modeling biological vision and brain information processing. *Annual review of vision science*, 1:417–446, 2015.

Elizabeth A Krupinski. Current perspectives in medical image perception. *Attention, Perception, & Psychophysics*, 72(5):1205–1217, 2010.

Jonas Kubilius, Martin Schrimpf, Aran Nayebi, Daniel Bear, Daniel LK Yamins, and James J DiCarlo. Cornet: Modeling the neural mechanisms of core object recognition. *BioRxiv*, pp. 408385, 2018.

Phuc H Le-Khac, Graham Healy, and Alan F Smeaton. Contrastive representation learning: A framework and review. *Ieee Access*, 8:193907–193934, 2020.

Victor Lempitsky. Autoencoder. *Computer Vision: A Reference Guide*, pp. 1–6, 2019.

Jeremiah Liu, Zi Lin, Shreyas Padhy, Dustin Tran, Tania Bedrax Weiss, and Balaji Lakshminarayanan. Simple and principled uncertainty estimation with deterministic deep learning via distance awareness. *Advances in neural information processing systems*, 33:7498–7512, 2020a.

Jialun Liu, Yifan Sun, Chuchu Han, Zhaopeng Dou, and Wenhui Li. Deep representation learning on long-tailed data: A learnable embedding augmentation perspective. In *Proceedings of the IEEE/CVF conference on computer vision and pattern recognition*, pp. 2970–2979, 2020b.

Weiyang Liu, Yandong Wen, Zhiding Yu, Ming Li, Bhiksha Raj, and Le Song. Sphereface: Deep hypersphere embedding for face recognition. In *Proceedings of the IEEE conference on computer vision and pattern recognition*, pp. 212–220, 2017.

Xiaoqiang Lu, Wuxia Zhang, and Ju Huang. Exploiting embedding manifold of autoencoders for hyperspectral anomaly detection. *IEEE Transactions on Geoscience and Remote Sensing*, 58(3): 1527–1537, 2019.

Xuanwen Luo, Qiang Cheng, and Joseph Tan. A lossless data embedding scheme for medical images in application of e-diagnosis. In *Proceedings of the 25th Annual International Conference of the IEEE Engineering in Medicine and Biology Society (IEEE Cat. No. 03CH37439)*, volume 1, pp. 852–855. IEEE, 2003.

Lingheng Meng, Shifei Ding, and Yu Xue. Research on denoising sparse autoencoder. *International Journal of Machine Learning and Cybernetics*, 8:1719–1729, 2017.

Tomas Mikolov, Kai Chen, Greg Corrado, and Jeffrey Dean. Efficient estimation of word representations in vector space. *arXiv preprint arXiv:1301.3781*, 2013.

Peter CM Molenaar and Cynthia G Campbell. The new person-specific paradigm in psychology. *Current directions in psychological science*, 18(2):112–117, 2009.

Jishnu Mukhoti, Andreas Kirsch, Joost van Amersfoort, Philip HS Torr, and Yarin Gal. Deterministic neural networks with inductive biases capture epistemic and aleatoric uncertainty. *arXiv preprint arXiv:2102.11582*, 2, 2021.

Robert M Nosofsky, Craig A Sanders, Brian J Meagher, and Bruce J Douglas. Toward the development of a feature-space representation for a complex natural category domain. *Behavior research methods*, 50:530–556, 2018.

Simone Palazzo, Concetto Spampinato, Isaak Kavasidis, Daniela Giordano, Joseph Schmidt, and Mubarak Shah. Decoding brain representations by multimodal learning of neural activity and visual features. *IEEE Transactions on Pattern Analysis and Machine Intelligence*, 43(11):3833–3849, 2020.

Adam Paszke, Sam Gross, Francisco Massa, Adam Lerer, James Bradbury, Gregory Chanan, Trevor Killeen, Zeming Lin, Natalia Gimelshein, Luca Antiga, Alban Desmaison, Andreas Kopf, Edward Yang, Zachary DeVito, Martin Raison, Alykhan Tejani, Sasank Chilamkurthy, Benoit Steiner, Lu Fang, Junjie Bai, and Soumith Chintala. Pytorch: An imperative style, high-performance deep learning library.

Joshua C Peterson, Joshua T Abbott, and Thomas L Griffiths. Evaluating (and improving) the correspondence between deep neural networks and human representations. *Cognitive science*, 42 (8):2648–2669, 2018.

Hieu H Pham, Tung T Le, Dat Q Tran, Dat T Ngo, and Ha Q Nguyen. Interpreting chest x-rays via cnns that exploit hierarchical disease dependencies and uncertainty labels. *Neurocomputing*, 437: 186–194, 2021.

Michael Psenka, Druv Pai, Vishal Raman, Shankar Sastry, and Yi Ma. Representation learning via manifold flattening and reconstruction. *Journal of Machine Learning Research*, 25(132):1–47, 2024.

Brett D Roads and Bradley C Love. Modeling similarity and psychological space. *Annual Review of Psychology*, 75:215–240, 2024.

Téo Sanchez, Baptiste Caramiaux, Pierre Thiel, and Wendy E Mackay. Deep learning uncertainty in machine teaching. In *27th International Conference on Intelligent User Interfaces*, pp. 173–190, 2022.

Florian Schroff, Dmitry Kalenichenko, and James Philbin. Facenet: A unified embedding for face recognition and clustering. In *Proceedings of the IEEE conference on computer vision and pattern recognition*, pp. 815–823, 2015.

Priya Tarigopula, Scott Laurence Fairhall, Anna Bavaresco, Nhut Truong, and Uri Hasson. Improved prediction of behavioral and neural similarity spaces using pruned dnns. *Neural Networks*, 168: 89–104, 2023.

Michael Tschannen, Olivier Bachem, and Mario Lucic. Recent advances in autoencoder-based representation learning. *arXiv preprint arXiv:1812.05069*, 2018.

Laurens Van der Maaten and Geoffrey Hinton. Visualizing data using t-sne. *Journal of machine learning research*, 9(11), 2008.

Jian Wang, Feng Zhou, Shilei Wen, Xiao Liu, and Yuanqing Lin. Deep metric learning with angular loss. In *Proceedings of the IEEE international conference on computer vision*, pp. 2593–2601, 2017.

Wei Wang, Yan Huang, Yizhou Wang, and Liang Wang. Generalized autoencoder: A neural network framework for dimensionality reduction. In *Proceedings of the IEEE conference on computer vision and pattern recognition workshops*, pp. 490–497, 2014.

Kilian Q Weinberger and Lawrence K Saul. Distance metric learning for large margin nearest neighbor classification. *Journal of machine learning research*, 10(2), 2009.

Kilian Q Weinberger, John Blitzer, and Lawrence Saul. Distance metric learning for large margin nearest neighbor classification. *Advances in neural information processing systems*, 18, 2005.

Michael Wilber, Iljung Kwak, and Serge Belongie. Cost-effective hits for relative similarity comparisons. In *Proceedings of the AAAI Conference on Human Computation and Crowdsourcing*, volume 2, pp. 227–233, 2014.

Eric Xing, Michael Jordan, Stuart J Russell, and Andrew Ng. Distance metric learning with application to clustering with side-information. *Advances in neural information processing systems*, 15, 2002.

Zheng Yang, Binbin Xu, Wei Luo, and Fei Chen. Autoencoder-based representation learning and its application in intelligent fault diagnosis: A review. *Measurement*, 189:110460, 2022.

Matthew D Zeiler and Rob Fergus. Visualizing and understanding convolutional networks. In *Computer Vision–ECCV 2014: 13th European Conference, Zurich, Switzerland, September 6-12, 2014, Proceedings, Part I 13*, pp. 818–833. Springer, 2014.

Richard Zhang, Phillip Isola, Alexei A Efros, Eli Shechtman, and Oliver Wang. The unreasonable effectiveness of deep features as a perceptual metric. In *Proceedings of the IEEE conference on computer vision and pattern recognition*, pp. 586–595, 2018.

A Appendix

A.1 Subject characteristics

The subjects were randomly assigned to either Group A or Group B. The mean ages of subjects in Groups A and B were 31 years (SD = 5.9 years) and 36.6 years (SD = 6.4 years), respectively. The number of female participants in Groups A and B were 3 and 6, respectively. Table 3 provides information for each participant, however, to protect participant anonymity, gender and specific clinical backgrounds are not indicated.

* GP1: General physician without clinical training, GP2: General physician with internship traning, SP1: Specialist in internal medicine, SP2: Specialist in chest X-ray-related disciplines (anesthesiology, thoracic surgery, occupational medicine, family medicine, pediatrics, emergency medicine, radiology, radiation oncology, nuclear medicine), SP3 : Other specialists (otorhinolaryngology, rehabilitation medicine, ophthalmology, orthopedic surgery, obstetrics and gynecology, neurology, dermatology, plastic surgery, neurosurgery)

A.2 Model archtecture

We implemented our model using Python version 3.8.18 and the PyTorch(Paszke et al.) version 2.2.1 library on the Ubuntu 18.0 environment. Please refer to Fig. 7 for the logical structure of the model. The random seed used for the final model selection and the conda virtual environment configuration are provided in the attached files.

A.3 Computer resources

All models were trained using a single RTX 3090 GPU. We were able to train 10 models simultaneously on a single GPU. Although our individual models are relatively small in scale, they must be trained separately for each subject. We utilized 4 GPUs concurrently to perform parallel computations for multiple models. Training the same model 20 times with different random seeds allowed us to select the optimal model. The time required to train a single model ranged from approximately 3.5 to 5.5 hours.

Table 3: Key information of the subjects

Group A			Group B		
Subject ID	Age	Clinical field*	Subject ID	Age	Clinical field*
1	45	SP2	63	38	SP4
2	39	SP2	64	44	GP2
3	33	SP2	65	38	SP2
4	34	SP2	66	36	SP2
5	32	SP2	67	39	SP3
6	34	SP3	68	37	SP1
7	33	SP3	69	39	SP3
8	32	SP3	70	40	SP3
9	33	GP1	71	34	SP3
10	32	SP2	72	36	SP3
11	30	SP2	73	34	SP1
12	31	SP2	74	33	SP3
13	29	SP2	75	43	SP2
14	30	SP2	76	38	SP2
15	32	SP3	77	32	SP1
16	29	SP2	78	36	SP3
17	33	SP2	79	35	SP1
18	32	GP2	80	36	SP2
19	29	GP2	81	36	SP3
20	29	GP2	82	41	SP2
21	32	GP1	83	35	SP1
22	30	GP1	84	35	SP1
23	28	GP1	85	32	SP2
24	26	GP2	86	32	GP1
25	31	GP1	87	32	SP3
26	27	GP2	88	31	SP3
27	29	GP2	89	30	GP1
28	27	GP2	90	30	SP1
29	29	SP2	91	32	SP2
30	28	GP1	92	38	GP2
31	28	GP1	93	36	SP2
32	28	GP1	94	35	GP2
33	27	GP2	95	34	SP1
34	29	GP1	96	30	GP1
35	27	GP2	97	30	GP2
36	31	GP1	98	33	GP1
37	26	GP1	99	41	SP2
38	28	GP2	100	32	GP1
39	27	GP2	101	33	GP2
40	30	GP1	102	32	GP1
41	28	GP1	103	32	GP1
42	28	GP2	104	37	GP2
43	30	GP1	105	26	GP2
44	30	GP1	106	30	SP2
45	27	GP2	107	27	GP2
46	30	GP1	108	26	GP1
47	26	GP2	109	38	GP2
48	28	GP1	110	26	GP1
49	26	GP2	111	52	SP2
50	26	GP1	112	58	SP2
51	27	GP2	113	47	SP2
52	25	GP1	114	44	SP2
53	27	SP3	115	45	SP2
54	27	GP2	116	46	SP1
55	33	SP3	117	44	SP1
56	26	GP1	118	46	SP1
57	27	GP1	119	44	SP1
58	55	SP1	120	42	SP3
59	48	SP2	121	40	SP2
60	46	SP2			
61	44	SP2			
62	42	SP2			

A.4 MAIN EXPERIMENTS (SIMILARITY JUDGEMENTS)

This section describes the main human behavior experiment, focusing on the procedures presented to the participants. Each instance in the main experiment consists of a triplet, composed of three images. At the start of each instance(Fig. 8), the three images forming the triplet are displayed on the left side of the screen (Fig. 9). Each image is matched with a drag ball of a different color. The order of tasks and the arrangement of images within each task are randomized for each subject. In the center of the screen, the matched drag balls are initially arranged in an equilateral triangle.

Participants are asked to drag the balls such that the matched images are positioned closer together as their perceived similarity increases (Fig. 10). If two images are perceived as identical at embedding level, participants should place the corresponding balls in the same position. After submitting

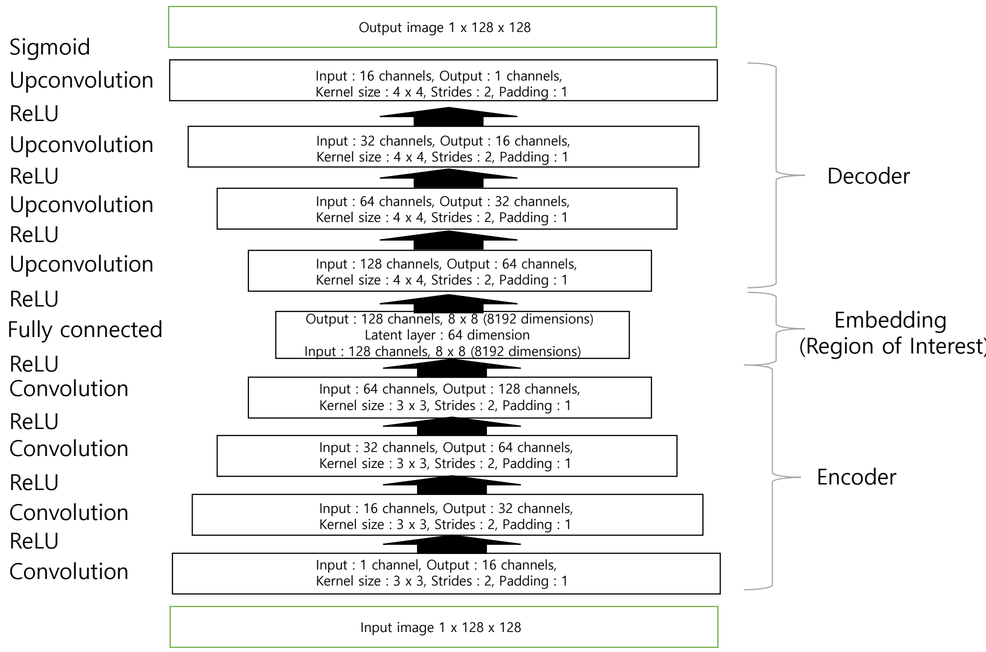

Figure 7: Architecture of our neural network model.

their similarity judgments, participants can input their confidence in the similarity between each pair of drag balls (Fig. 11). Clicking on the line connecting two drag balls changes its thickness, with thicker lines indicating higher confidence levels, measured on a 5-point scale. Although the confidence measurements are provided in the attachment files, they were not included in the analysis for this experiment.

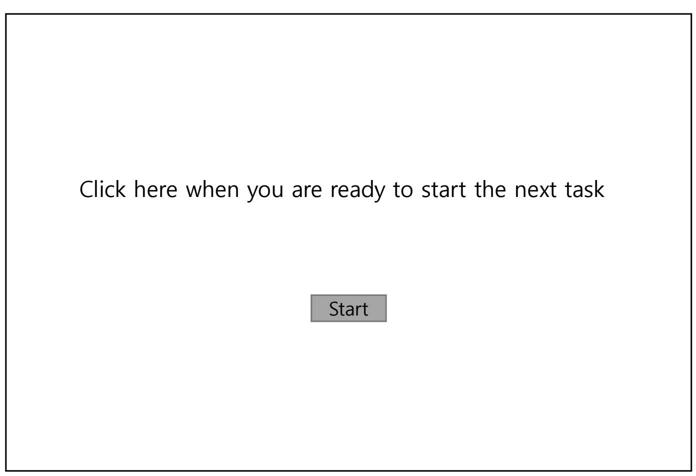

Figure 8: Screen image before start each task.

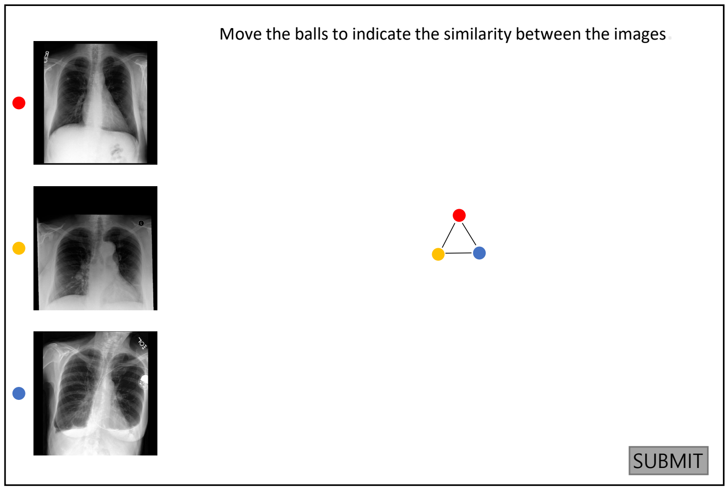

Figure 9: Initial task image.

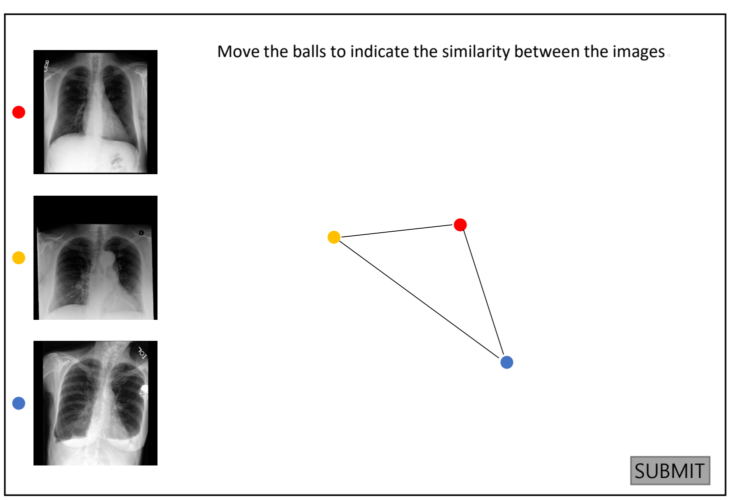

Figure 10: Subject's Ball Movement.

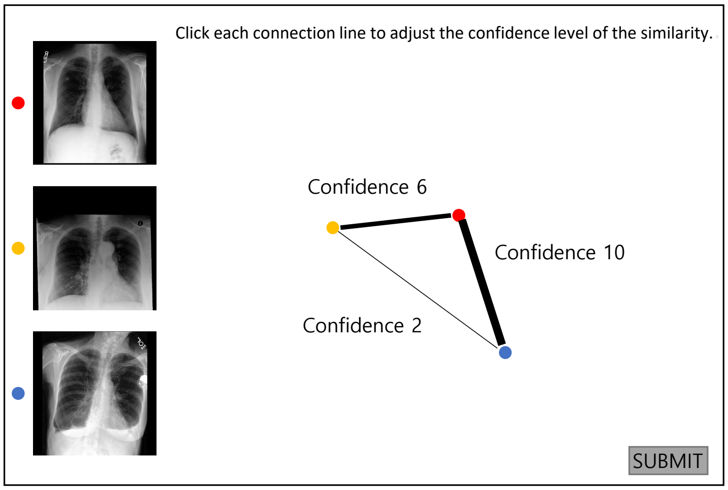

Figure 11: Input confidence level for each similarity judgements.

A.5 Detail results of main study (similarity inference)

Tables 4 and 5 present the similarity inference performance of models generated in Group A and Group B, respectively, displaying Specific Performance (SP) and Non-Specific Performance (NSP) for each model. These tables include inference results for models trained using our proposed standard approach as well as two ablation settings. SP is reported as the mean and standard deviation of the performance across multiple models generated through cross-validation. However, it should be noted that the error presented for NSP is the standard error of the inference performance for all subjects except the targeted subject for the model. This distinction is made to clearly highlight the characteristics of the raw performance information used to calculate NSP across different subjects.

Table 4: Performance of each model for group A (Accuracy and Standard deviation: %)

	Our mothods		Excluding reconstruction loss		Excluding triplet loss	
Subject ID	SP	NSP	SP	NSP	SP	NSP
1	67.7±3.3	59.1±9.6	44.3±31.	59.4±7.8	60.7±4.1	59.3±8.9
2	65.0±1.4	57.8±8.4	33.3±24.	48.6±8.2	57.3±10.	62.7±9.9
3	69.7±2.9	51.1±7.1	55.0±1.4	45.3±10.	63.0±0.0	59.7±9.4
4	67.3±1.9	61.2±9.3	55.3±4.1	51.5±9.7	55.0±1.4	53.4±8.1
5	58.3±5.6	54.5±7.6	55.3±4.1	56.6±10.	54.3±11.	54.3±9.5
6	66.3±2.9	55.1±9.0	50.7±5.6	57.2±8.1	54.0±13.	56.4±8.3
7	68.7±4.2	52.6±9.1	55.3±12.	54.3±7.5	59.7±2.9	56.3±8.6
8	62.7±4.7	57.1±9.6	51.7±10.	53.9±6.6	58.3±3.3	53.8±8.0
9	66.3±2.9	44.1±8.3	34.0±24.	49.2±9.6	64.0±7.0	52.3±9.4
10	64.3±4.2	53.1±7.8	60.7±6.6	49.3±9.7	54.0±5.9	54.4±9.8
11	71.0±1.4	58.9±9.4	58.7±8.4	55.7±9.1	64.0±5.9	60.6±9.5
12	67.7±3.3	55.7±8.9	57.3±1.9	49.9±8.7	66.0±8.2	54.7±9.9
13	71.0±1.4	58.0±8.5	49.7±5.3	54.6±8.3	55.3±4.1	62.7±8.7
14	69.7±2.9	52.3±9.4	57.3±10.	49.6±10.	57.7±5.6	52.2±8.5
15	69.7±2.9	58.0±10.	31.0±24.	56.2±8.3	61.7±12.	56.0±8.1
16	67.3±1.9	52.5±10.	47.3±6.1	51.0±7.0	58.7±4.2	51.7±9.9
17	66.0±0.0	52.1±9.1	48.7±6.1	53.2±8.0	55.0±7.0	62.7±8.7
18	69.3±4.7	47.6±7.6	35.3±29.	60.7±10.	57.3±4.2	58.3±9.3
19	64.0±1.4	51.3±8.5	56.0±8.2	54.9±9.4	56.7±4.7	51.8±9.5
20	75.3±3.3	50.3±7.1	52.0±13.	56.5±8.6	53.0±5.7	64.0±10.
21	72.0±7.0	54.2±9.1	60.7±3.3	53.5±9.3	59.7±7.4	56.3±8.9
22	67.3±6.1	58.4±9.8	48.7±11.	52.3±9.4	48.7±4.2	51.4±8.3
23	62.0±2.8	58.6±8.6	59.7±7.4	51.1±7.2	61.0±1.4	56.2±8.5
24	69.7±2.9	63.9±9.2	58.7±1.9	51.8±7.8	61.7±8.0	59.2±9.6
25	72.0±2.8	65.1±9.1	62.0±2.8	55.4±8.2	59.7±5.3	54.9±8.8
26	74.0±5.9	58.5±8.4	62.0±5.9	55.1±9.6	66.3±7.4	59.8±9.1
27	72.0±1.4	54.9±8.5	57.3±1.9	47.3±8.2	64.3±4.2	53.7±7.8
28	64.3±6.1	61.5±8.5	48.3±5.6	56.3±7.3	50.7±12.	55.3±8.5
29	66.3±2.9	53.9±8.9	53.0±5.7	50.6±8.9	58.3±5.6	55.1±9.4
30	64.0±5.9	58.4±9.0	58.7±4.2	56.8±9.4	54.0±8.3	59.4±9.7
31	68.7±1.9	51.0±7.8	51.7±11.	58.1±8.5	63.0±7.3	59.9±8.0
32	64.0±2.8	55.7±9.5	55.0±8.3	51.9±10.	58.7±4.2	53.3±10.
33	69.7±4.7	49.4±7.2	47.7±5.6	55.2±8.3	64.3±4.2	58.4±8.9
34	69.7±7.4	57.0±9.4	56.3±5.3	55.2±9.4	59.3±9.4	55.4±9.4
35	69.7±2.9	53.2±8.8	64.3±4.2	54.6±7.5	58.7±1.9	53.6±9.7
36	68.3±3.3	52.6±8.9	54.3±10.	53.0±8.9	60.7±8.8	63.4±9.1
37	66.3±2.9	56.8±9.0	55.0±7.0	55.0±8.0	58.7±4.2	60.7±9.0
38	68.7±4.2	52.8±9.5	55.3±7.5	56.2±10.	56.3±2.9	51.7±8.9
39	67.3±4.2	56.2±7.7	57.7±13.	57.7±8.6	55.0±7.0	49.8±10.
40	69.7±2.9	53.7±10.	62.0±2.8	54.6±9.7	57.3±8.4	60.4±10.
41	68.3±5.6	53.3±7.5	60.7±10.	59.8±9.2	65.3±8.8	55.4±8.2
42	68.7±1.9	58.9±9.5	62.0±5.9	57.3±10.	58.3±3.3	63.6±9.2
43	74.0±7.0	52.5±9.2	60.7±8.8	57.3±9.8	78.7±6.1	63.3±9.0
44	68.3±3.3	57.4±7.8	62.0±1.4	57.1±9.0	50.7±4.1	54.4±7.8
45	64.0±1.4	55.4±9.4	55.3±4.1	50.9±10.	51.7±6.1	62.8±8.7
46	68.3±3.3	53.7±8.5	58.7±6.6	62.6±9.1	57.3±6.6	56.2±8.4
47	65.0±1.4	60.2±10.	31.0±22.	47.0±9.7	40.7±5.6	56.5±9.3
48	65.0±1.4	50.9±8.9	57.7±3.3	46.0±8.3	58.3±8.8	54.9±8.8
49	68.7±4.2	57.7±10.	54.3±4.2	55.3±8.9	53.0±12.	50.3±7.6
50	70.7±3.3	53.6±9.8	49.7±2.9	52.7±9.1	50.7±4.1	55.4±8.4
51	67.3±1.9	57.8±9.0	54.3±6.1	56.3±8.2	57.3±12.	54.8±9.4
52	66.7±4.7	51.9±10.	68.3±3.3	59.9±8.5	54.0±2.8	52.9±7.6
53	62.0±5.9	60.5±8.8	54.0±8.3	48.4±8.5	43.0±15.	54.9±9.6
54	74.0±5.9	58.5±8.4	62.0±5.9	55.1±9.6	66.3±7.4	59.8±9.1
55	68.7±4.2	52.6±9.1	55.3±12.	54.3±7.5	59.7±2.9	56.3±8.6
56	72.0±5.9	58.4±10.	56.3±2.9	54.8±9.3	56.7±9.4	55.7±8.3
57	67.7±8.8	57.0±8.6	53.0±12.	52.0±8.5	59.7±4.7	56.2±8.5
58	72.0±7.0	61.3±8.6	59.7±2.9	54.0±9.7	68.7±10.	60.9±9.4
59	67.7±3.3	55.6±8.6	58.7±6.6	48.5±8.6	51.7±8.0	56.2±8.5
60	66.3±7.4	56.1±8.6	63.0±7.3	46.1±9.5	47.3±4.2	54.1±8.6
61	71.7±4.2	48.7±7.8	51.0±1.4	57.0±10.	58.7±4.2	59.4±9.3
62	66.7±4.7	59.7±10.	39.7±28.	54.6±9.5	64.3±6.1	62.5±8.6

Table 5: Performance of each model for group B (Accuracy and Standard deviation: %)

	Our mothods		Excluding reconstruction loss		Excluding triplet loss	
Subject ID	SP	NSP	SP	NSP	SP	NSP
63	72.0±8.6	63.0±8.4	54.0±5.9	53.9±8.9	62.0±8.3	58.4±8.9
64	68.3±5.6	59.1±8.5	59.7±11.	52.7±8.2	64.0±2.8	62.8±9.7
65	71.0±1.4	57.5±7.6	65.3±4.1	58.4±7.9	63.0±5.7	55.3±9.0
66	67.7±8.8	57.0±9.0	54.0±2.8	42.8±8.6	61.0±8.3	60.1±8.9
67	68.7±4.2	63.9±8.9	51.7±4.2	54.7±8.6	65.3±8.8	60.6±8.2
68	71.7±6.1	60.3±9.3	56.7±4.7	59.7±8.4	67.3±4.2	62.2±9.2
69	68.7±4.2	57.1±8.6	55.0±7.0	51.6±8.4	65.0±7.0	53.6±9.5
70	68.7±4.2	52.1±7.9	56.3±9.4	58.2±10.	64.3±4.2	52.9±8.2
71	68.7±4.2	58.4±9.1	49.7±10.	59.1±9.0	62.7±4.7	55.9±10.
72	68.7±6.6	54.7±8.2	55.3±7.5	48.2±10.	50.7±14.	60.0±7.5
73	66.3±2.9	54.9±7.1	63.3±4.7	62.2±8.5	61.7±4.2	60.9±9.2
74	73.0±2.4	60.6±8.0	49.7±5.3	54.2±8.6	63.0±9.6	62.5±9.3
75	65.3±3.3	59.4±6.9	70.0±8.2	59.8±8.5	62.7±4.7	61.9±9.5
76	67.3±6.6	58.6±9.1	56.3±4.7	52.6±7.4	58.7±4.2	54.4±9.0
77	70.7±4.1	64.8±8.0	60.7±7.5	58.9±10.	64.3±4.2	57.7±7.9
78	65.0±1.4	59.9±8.5	53.0±7.3	47.2±8.3	56.3±7.4	61.1±8.1
79	67.7±3.3	57.5±7.6	51.0±15.	62.2±8.6	58.3±5.6	62.0±9.0
80	68.7±1.9	56.8±9.0	57.7±11.	61.7±8.5	65.3±4.1	59.1±8.5
81	67.7±5.6	58.4±8.7	58.7±8.4	56.9±10.	60.0±14.	61.0±8.0
82	69.3±4.7	56.1±8.5	48.7±9.8	58.6±8.6	58.7±6.1	61.6±9.9
83	65.0±1.4	48.9±7.8	55.0±9.4	58.7±8.2	59.7±2.9	61.0±9.2
84	71.0±1.4	60.5±8.1	56.3±7.4	52.1±9.7	60.7±6.6	60.5±8.2
85	67.3±1.9	55.9±7.8	52.7±4.7	47.8±8.4	59.3±4.7	61.5±9.8
86	64.0±1.4	60.6±8.1	53.0±5.7	52.1±8.1	64.3±6.1	56.4±9.0
87	68.3±5.6	55.9±8.6	59.7±5.3	60.7±9.3	58.7±9.8	63.2±8.9
88	64.0±1.4	56.9±10.	58.7±9.8	59.9±8.0	49.3±4.7	54.7±8.8
89	66.3±5.3	62.0±9.2	48.7±11.	50.5±9.1	53.0±13.	62.6±9.4
90	69.7±2.9	49.1±8.4	56.3±5.3	52.6±8.4	59.7±2.9	59.0±10.
91	70.7±3.3	59.4±8.6	49.3±4.7	54.8±9.8	65.0±9.4	62.8±7.8
92	67.3±4.2	52.1±9.4	54.0±16.	60.1±8.3	61.7±4.2	57.5±8.9
93	73.0±5.7	55.7±7.8	57.7±3.3	42.7±8.7	65.3±11.	53.5±9.3
94	74.0±7.0	61.5±8.2	66.3±2.9	59.8±7.9	67.7±5.6	63.1±8.8
95	70.7±4.1	58.2±8.5	44.0±8.6	59.0±9.0	72.0±2.8	63.6±8.0
96	68.7±1.9	58.3±7.1	63.3±4.7	51.3±8.7	66.3±4.7	60.5±9.5
97	66.3±2.9	50.9±8.5	56.3±4.7	58.9±9.9	65.3±4.1	62.2±7.8
98	68.3±5.6	60.7±10.	49.7±2.9	51.7±8.9	67.7±10.	62.1±8.9
99	65.3±8.8	57.9±8.1	60.7±7.5	50.6±9.7	56.7±9.4	59.9±8.9
100	67.3±1.9	59.7±9.4	53.0±2.4	50.6±7.8	67.3±8.4	61.0±9.4
101	73.0±5.7	58.6±8.4	48.7±9.8	57.6±8.6	63.3±4.7	61.0±8.8
102	73.3±4.7	57.8±9.2	58.3±10.	55.8±10.	62.0±5.9	62.0±9.0
103	73.0±2.4	61.8±8.2	50.0±8.2	54.1±8.7	68.3±3.3	52.6±9.2
104	69.7±9.7	56.7±8.8	55.0±9.4	57.2±10.	75.0±1.4	61.7±9.5
105	66.3±5.3	62.5±9.4	54.0±8.6	59.1±9.4	66.0±14.	62.1±9.8
106	74.0±1.4	52.2±9.4	64.3±8.0	57.4±7.7	64.0±13.	62.9±9.2
107	71.0±1.4	58.3±10.	56.3±4.7	56.7±7.3	66.3±4.7	62.7±9.5
108	66.3±2.9	48.8±9.1	49.7±10.	52.1±7.6	65.3±4.1	57.8±7.8
109	68.7±1.9	55.5±9.1	55.3±5.6	50.5±8.2	58.7±9.8	55.4±8.2
110	68.7±4.2	56.7±8.5	56.3±9.4	55.8±8.4	54.3±10.	60.5±8.4
111	68.3±3.3	59.4±8.2	59.7±7.4	49.8±7.7	65.3±5.6	60.2±9.6
112	70.7±4.1	52.4±7.9	56.7±9.4	57.2±7.7	54.3±11.	60.0±7.5
113	70.7±3.3	52.4±9.5	58.3±8.8	49.4±8.9	64.0±2.8	62.8±9.7
114	72.0±1.4	65.4±7.7	50.7±10.	45.5±8.5	59.7±5.3	58.5±8.1
115	68.7±1.9	55.9±8.9	62.0±9.4	55.6±9.7	60.7±5.6	65.5±8.5
116	66.3±2.9	55.3±8.3	55.3±13.	61.2±10.	60.7±3.3	53.8±9.8
117	64.3±8.0	56.3±7.6	57.3±9.8	62.6±8.8	60.7±8.8	60.3±8.2
118	71.7±4.2	54.4±7.7	50.7±13.	54.9±8.9	63.0±12.	61.2±8.8
119	67.7±3.3	50.9±8.5	52.0±15.	59.2±8.7	58.3±8.8	59.3±8.6
120	69.7±2.9	52.2±9.2	59.7±7.4	56.3±8.5	58.7±1.9	62.1±9.0
121	61.7±4.2	58.7±9.3	56.3±2.9	55.0±7.7	71.7±4.2	53.3±9.3

A.6 Pseudo-code for qualitative analysis

This pseudo-code summarizes the algorithm for selecting annotation pixels of the model in Section 4.6 of the main text.

Algorithm 1 Identify key pixels based on embedding variance

Input: Embedding function $E(\cdot)$, Separated reference dataset D, Test image e, Number of repetitions N
Output: Top 10 key pixels

Step 1: Compute variances for each embedding Dimension
for each image $d \in D$ **do**
    Compute embedding $E(d)$
end for
Compute variance for each embedding dimension
Determine reference unit as the dimension with the highest variance

Step 2: Analyze each pixel in test image e
for each pixel (i, j) in e **do**
    L : Empty list
    for $k = 1$ to N **do**
        $E(e_{noisy}$: Add random noise to pixel (i, j) in e
        Compute embedding $E(e_{noisy}$
        Append reference unit output to L
    end for
    Compute variance of the L
end for

Step 3: Identify top 10 key pixels
Select top 10 pixels with the highest variance in L
Return Top 10 key pixels

A.7 Hyperparameter Sensitivity Analysis

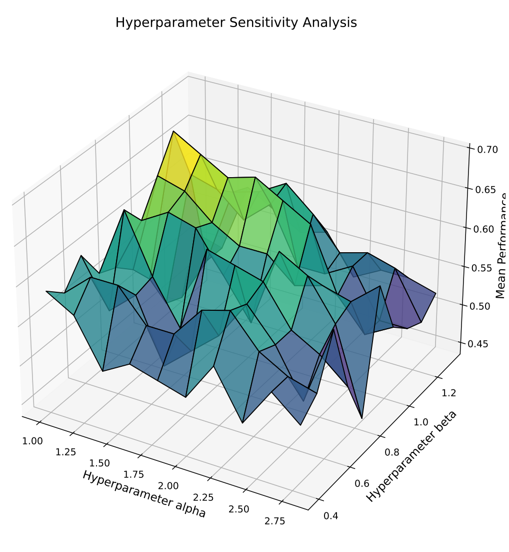

Figure 12: Sensitivity Analysis of Average Predictive Performance for Hyperparameters α and β.

The hyperparameters α and β, introduced in Section 4.4 of the main text, were determined through a preliminary sensitivity analysis using data from five subjects. α values were varied discretely between 1.0 and 2.0, and β values between 0.4 and 1.3, generating a total of 100 parameter combinations for testing. Refer to Fig. 12. As a result, the highest average predictive performance of 0.7 was observed at α = 1.2 and β = 1.0, which were selected as the optimal hyperparameters.

A.8 Test-Retest Analysis of Similarity Pattern Vectors

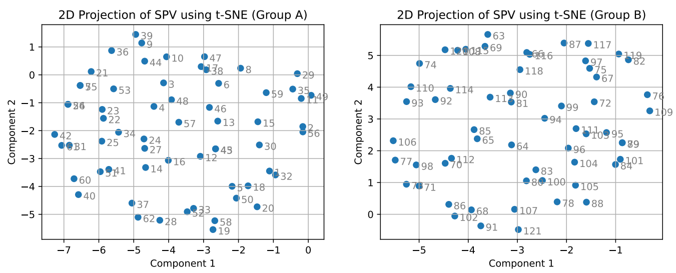

(a)

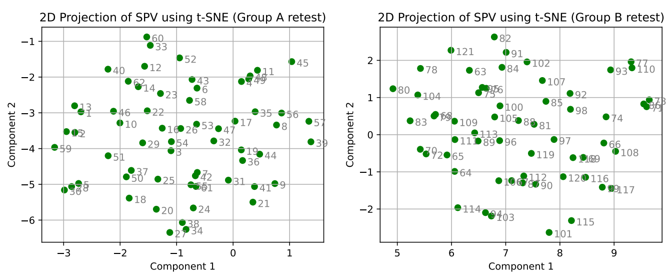

(b)

Figure 13: Results of the test-retest analysis for similarity pattern analysis across all subjects with 15 triplets. (a) 2D t-SNE visualization of similarity pattern vectors obtained from the initial sampling. (b) 2D t-SNE visualization of similarity pattern vectors obtained from the delayed sampling.

The SPVs (Similarity Pattern Vectors) of each subject were measured through behavioral experiments. To validate the reliability of similarity pattern sampling, we compared the SPVs obtained from re-sampling conducted at different time intervals. Behavioral sampling was performed for 1,500 triplets per subject, with 15 triplets randomly re-sampled during the experiment (Retest) to assess subject consistency. The SPVs generated for each subject from two samplings of the same 15 triplets were then compared. While some subjects exhibited varying responses to the same triplets, their SPVs were observed to cluster closely with those of similar subjects during the Retest. This finding suggests that subjects demonstrated high response consistency even when re-sampling was conducted after a temporal delay.